JMEPEG (2022) 31:825–832
https://doi.org/10.1007/s11665-021-06216-y

1059-9495/$19.00

Material Characterization and Modeling for Finite Element Simulation of Press Hardening with AISI 420C

Bernd-Arno Behrens, Daniel Rosenbusch, Hendrik Wester, and Eugen Stockburger

Submitted: 11 May 2021 / Revised: 20 August 2021 / Accepted: 27 August 2021 / Published online: 16 September 2021

The process of press hardening is gaining importance in view of the increasing demand for weight reduction combined with higher crash safety in cars. An alternative to the established manganese-boron steel 22MnB5 is hot-formed martensitic chromium steels such as AISI 420C. Strengths of 1850 MPa and elongations of 12% are possible, exceeding those of 22MnB5. In industrial manufacturing, FE-simulation is commonly used in order to design car body parts cost-efficiently. Therefore, the characterization and the modeling of AISI 420C regarding flow stress, phase transformations as well as failure behavior are presented in this paper. Temperature-depended flow curves are determined, showing the low flow stress and hardening behavior at temperatures around 1000 °C. Cooling experiments are carried out, and a continuous cooling diagram is generated. Observed phases are martensite and retained austenite for industrial relevant cooling rates above 10 K/s. In addition, tests to investigate temperature-dependent forming limit curves are performed. As expected, the highest forming limit is reached at 1050 °C and decreases with falling temperature. Finally, a simulation model of a press-hardening process chain is set up based on the material behavior characterized earlier and compared to experimental values. The forming force, phase transformation and forming limit could be calculated with good agreement to the experiment.

Keywords continuous cooling diagram, flow curve, forming limit diagram, martensitic chromium steel, press hardening simulation

1. Introduction

Recently, major focus in the automotive industry has been on reducing energy consumption and emissions while improving crashworthiness as well as driving safety. This can be achieved by reducing vehicle weight using materials with high strength to weight ratio (Ref 1). Press hardening, also known as hot stamping, is a combination of hot forming and heat treatment within the forming dies (Ref 2). Ultra high-strength steels like 22MnB5 can be formed into complex shapes, which is not possible with regular cold-forming operations. Press-hardened components in the automotive industry are chassis components like A-pillar, B-pillar, bumper, roof rail, rocker rail and tunnel. The martensitic chromium steel AISI 420C offers the potential to improve these safety-relevant components currently made of 22MnB5 (Ref 3). For press hardening AISI 420C, the blank is brought to an austenitizing temperature of 1150 °C and soaked for 5 min to achieve homogeneous austenite (Ref 3). After the heat treatment, the blank is transferred to the forming press. Subsequently, it is deep-drawn and cooled inside the tools. In order to set the final mechanical properties for AISI 420C, the part is finally tempered. The thermal process route is shown in Fig. 1. Tensile strength and fracture elongation can be adjusted by tempering to values around 1850 MPa and 12% (Ref 3). Apart from the higher mechanical properties, AISI 420C has a lower critical cooling rate and a lower martensite start temperature, which is advantageous for subsequent operations after the forming step such as hot trimming. Disadvantages would be the higher material costs, the high austenitisation temperature and the additional process step due to tempering.

Nowadays, FE-simulation is often used as a numerical calculation method for designing hot forming processes (Ref 4). By this means, the number of time-consuming and costly experiments can be minimized in the design phase. Various

Abbreviations

$a_{1\text{-}6}$	Fitting parameters of the extrapolation approach
Ac_1	Austenite start temperature
Ac_3	Austenite finish temperature
β	Weighting parameter of the extrapolation approach
CCT	Continuous-cooling-transformation
ε_1	Major strain
ε_2	Minor strain
$\varepsilon_{1,limit}$	Major strain at failure
FLC	Forming limit curve
$k_{f,0}$	Yield strength
$k_{f,B}$	Extrapolation approach according to Birkert
$k_{f,HS}$	Extrapolation approach according to Hockett–Sherby
$k_{f,S}$	Extrapolation approach according to Swift
M	Martensite
n	Node
P	Pearlitic phase fraction
RA	Retained austenite
T	Present temperature
t	Time step
TTT	Time-temperature-transformation

Bernd-Arno Behrens, Daniel Rosenbusch, Hendrik Wester, and **Eugen Stockburger**, Institute of Forming Technology and Machines, Leibniz Universität Hannover, An der Universität 2, 30823 Garbsen, Germany. Contact e-mail: stockburger@ifum.uni-hannover.de.

studies were performed investigating the ongoing research of the press hardening process and its numerical simulation as several review papers indicate (Ref 5-7). The development of new approaches in modeling the phase transformation kinetics of press hardening began with the model of Akerström et al. (Ref 8), which was implemented in the commercial software code of LS Dyna. Müller et al. investigated the heat transfer coefficient during press hardening as a function of contact pressure and tool start temperature (Ref 9). A divisible stamping tool with welded thermocouples was used to measure the temperature, and the experiment was reproduced with an FE-model. The heat transfer coefficient was determined iteratively by comparing the numerical and experimental results. Venema et al. modeled friction in press hardening using a multi-scale friction model based on the surface characteristics of the sheet and tool (Ref 10). The friction model also takes important parameters like temperature, pressure and strain into account. A numerical study of contact conditions in press hardening for tool wear simulation was performed by Deng et al. (Ref 11). The influence of numerical factors such as the penalty value and mesh size on the contact conditions was investigated. A combination of hot metal gas forming and press hardening in one process step was investigated by Paul et al. (Ref 12). Hot tensile tests were used to create a material model for thermomechanical forming simulations. Based on a tube demonstrator, experimental and numerical studies were performed varying the forming temperature, internal pressure and pressure build-up rate. In Ref 13, Chen et al. analyzed and numerically modeled press hardening of a TA15 alloy. Phase transformations were investigated by means of continuous cooling tests, and a diffusion controlled phase transformation model was extended to describe the transformation kinetics of the titanium alloy. The transformation model was used in press hardening simulations and validated by experiments of a U-shape part. However, up to now no material models are available that can describe the temperature-dependent material behavior of AISI 420C with regard to flow stress, phase transformations and forming limit during press hardening. In this paper, material characterization and modeling methods are presented for the numerical simulation of hot forming and press hardening of martensitic chromium steel AISI 420C in 1.5 mm sheet thickness.

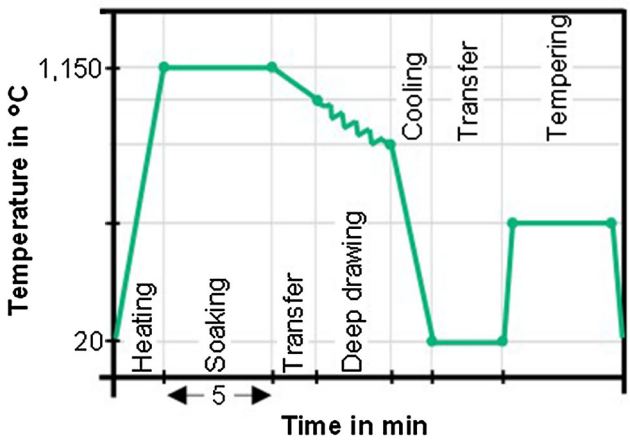

Fig. 1. Thermal process route

2. Material Characterization and Modeling Methods

2.1 Focus Areas Investigated in the Study

In order to be able to model a forming process numerically, among others flow curves of the material are required. Since the forming behavior is temperature-dependent, it needs to be characterized in the process-relevant temperature spectrum and modeled with a suitable extrapolation approach for higher plastic strains (Ref 14). The polymorphic transformation behavior of the microstructure in steel alloys is often described by CCT diagrams. A heated steel starts to transform its microstructure to austenite as soon as the temperature reaches the austenite start temperature Ac_1. If the temperature is higher than the austenite finish temperature Ac_3, only austenite is present in the material. CCT diagrams describe the transformation behavior of the steel during continuous cooling after the heating process. For the modeling of phase transformations in commercial FE-software, the Johnson–Mehl–Avrami equation is widely used for diffusion-controlled transformations (Ref 15) and the Koistinen–Marburger equation for diffusion-free transformations (Ref 16). These approaches can only be parameterized by isothermal processes. Hence, time-temperature-transformation (TTT) diagrams are required, which represent the transformation behavior after quenching and subsequent holding at a certain test temperature (Ref 17). Unfortunately, the determination of TTT diagrams is significantly more cost and time consuming than for CCT diagrams. However, each of these diagrams and therefore the transformation behavior of the steel strongly depend on the experimental boundary conditions such as the austenitisation temperature or soaking time. Thus, for an accurate prediction of the resulting phase fractions in an FE-simulation, the use of a TTT diagram for the exact process route is necessary. The use of forming limit curves (FLC) is state-of-the-art for the simulation-based prediction of material failure due to necking or fracture in sheet metal forming processes (Ref 18). An FLC indicates strain states in the plane of the sheet metal, which it can withstand without necking or fracturing, since, just like the flow stress, the forming capacity of a material depends on the temperature. However, conventional FLC recorded at room temperature according to ISO standard do not adequately describe the forming limit during hot sheet forming (Ref 19). Therefore, temperature-dependent FLC need to be recorded and implemented into the FE-software applied.

2.2 Flow Stress

To investigate the flow and hardening behavior of AISI 420C, miniature uniaxial tensile tests were carried out based on the standard ISO 6892 (Ref 20). The tests were performed on the quenching and forming dilatometer DIL 805A/D+T in tensile mode. The miniature tensile test specimens were cut by water jet from 1.5 mm thick sheets. Both, the forming dilatometer and the miniature tensile test specimen are shown in Fig. 2. For testing, the specimen was placed inside the heating coil and fixed in the two clamping tools. First, a heat treatment according to the industrial process chain from Fig. 1 was performed by inductive heating. Subsequently, the specimen was cooled to the forming temperature and isothermally tested until failure. The heating coil with integrated cooling system controlled the temperature of the specimen in the

middle of the 10 mm long gage area with thermocouples. The forming temperature was varied between 600 and 1100 °C with a strain rate of 0.1 s^{-1}. The forming force was applied by a hydraulic system and the change in length was measured by pushing rods.

The resulting force and the measured change in length were converted to uniaxial flow curves, as is the state-of-the-art. A combined extrapolation approach according to Birkert (Eq 1) was used to extend the flow curve data for higher plastic strains (Ref 14). The approach linearly weights the approaches of Swift (Eq 2) (Ref 21) and Hockett–Sherby (Eq 3) (Ref 22) with the weighting parameter β. By weighting the two approaches, the extrapolation is defined by high flexibility and more accuracy. The least squares method was used to determine the free parameters a_1 to a_6 as well as the weighting parameter β, whereby $k_{f,0}$ was set as the yield strength of the material.

$$k_{f,B} = \beta \cdot k_{f,S} + (1 - \beta) \cdot k_{f,HS} \quad \text{(Eq 1)}$$

$$k_{f,S} = a_1 \cdot (a_2 + \varepsilon)^{a_3} \quad \text{(Eq 2)}$$

$$k_{f,HS} = \left(a_4 - \left(a_4 - k_{f,0}\right) \cdot e^{a_5 \cdot \varepsilon^{a_6}}\right) \quad \text{(Eq 3)}$$

2.3 Phase Transformation

To investigate the transformation behavior of AISI 420C, CCT tests for cooling rates between 50 and 0.1 K/s were carried out on the dilatometer DIL 805A/D+T in quenching mode according to the standard ASTM A1033 (Ref 23). The cooling test specimens were produced by cutting from 5 mm thick sheet material. Both, the forming dilatometer in quenching mode and the test specimen used are shown in Fig. 3. The specimens were inductively heat-treated according to the process chain from Fig. 1 and cooled linearly with different cooling rates from 0.1 to 50 K/s using nitrogen. During the cooling of the specimens, the change in length was measured by the pushing rods as a function of the temperature. Based on the experimental data, the phase transformations were calculated according to ASTM A1033 and a CCT diagram was derived. Further, the austenite content retained was measured with the x-ray diffractometer XStress 3000. Based on the CCT diagram, a TTT diagram was generated with the software "TTT-CCT-diagram generator" of Transvalor. The generated TTT diagram was implemented in the Software Simufact Forming 16.0 to simulate the experimental CCT tests. The numerical and experimental length change-temperature-functions were compared, and the TTT diagram was shifted until both data agreed well. This method has earlier been used by Kock et al. (Ref 24) for TTT generation of 42CrMo4 and 100Cr6. By means of this method, a TTT diagram of AISI 420C was created in an efficient way.

2.4 Forming Limit

To investigate the material failure of AISI 420C for process-relevant temperatures, isothermal hot FLC tests were performed based on the standard ISO 12004 (Ref 25). For the experiments, five specimens according to Hasek were used to represent different strain states (Ref 26). The Hasek specimens were cut from 1.5 mm thick sheet material by water jet. The tests were carried out with a test setup applying a thermal container as well as gas pressure springs, which were installed in a servo-hydraulic forming simulator. In addition, the optical measuring system Aramis of GOM GmbH was used and adapted to the test setup. A detailed description of the test setup and the testing procedure is presented in (Ref 27). The thermal container, shown in Fig. 4, consisted of a drawing ring, a punch as well as a downholder and serves to maintain the forming temperature. To perform the hot FLC tests for AISI 420C, specimens shown in Fig. 4 were heated in a furnace according to the process route from Fig. 1. At the same time, the container was heated up to forming temperature in another furnace. The forming temperature was varied between 750 and 1050 °C. After heat treatment, the specimens were transferred from the first furnace to the thermal container in the second furnace. Subsequently, both were swiftly transferred and installed in the test setup. The thermal container and thus the specimens were clamped by gas pressure springs, and hereafter the forming simulator moved the punch into the thermal container. During the experiments, the z-displacement was measured by an optical measuring system using a stochastic pattern on the specimen surface. The major and minor strains could only be measured inaccurately due to the intense boundary conditions of the tests. Therefore, the major and minor strains were calculated by means of a numerical model. For this purpose, a digital twin was created based on the dimensions of the thermal container using the associated boundary conditions from the experiments. The experimental z-displacement measured with the optical measurement system at the time of failure was used in the simulation for defining the moment of material failure for each

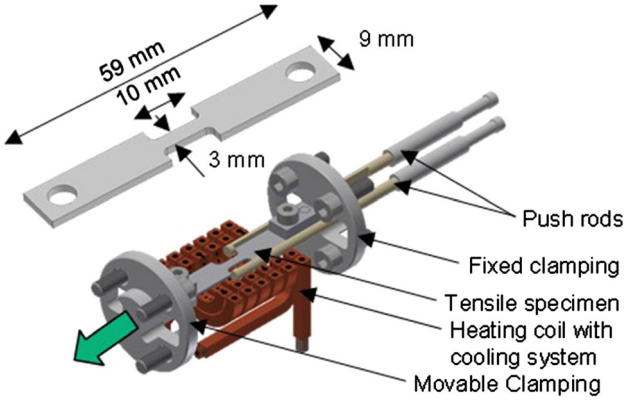

Fig. 2. Schematic representation of the miniature uniaxial tensile test specimen and the forming dilatometer in tensile mode

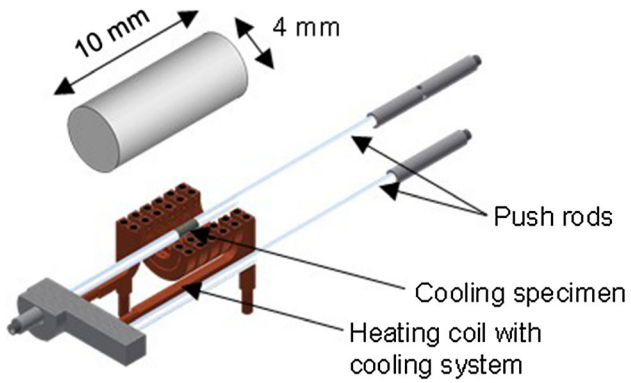

Fig. 3. Schematic representation of the cooling test specimen and the forming dilatometer in quenching mode

specimen geometry. Major and minor strains were analyzed in each specimen geometry to create the hot FLC. Using this experimental–numerical method, hot FLC for 750, 900 as well as 1050 °C were generated and implemented in Simufact Forming 16.0 by means of a user subroutine.

2.5 Validation Experiment and Numerical Simulation Model

To evaluate the material data and the modeling methods, two tensile test experiments were performed with the dilatometer in tensile mode. For both experiments, miniature tensile test specimen with a sheet thickness of 1.5 mm was used. In the first experiment, a specimen was heat-treated according to the process chain to validate the flow curves and the TTT diagram. Subsequently, it was cooled down from 1150 to 1050 °C with 15 K/s to reproduce the transfer process. It was hot-formed to a plastic strain of 0.2 with a forming speed of 0.1 mm/s and parallel-cooled to 750 °C to simulate a non-isothermal forming process. Finally, it was quenched to room temperature with a cooling rate of 20 K/s. In order to validate the FLC and the subroutine, a specimen was heat-treated, cooled down and non-isothermally hot-formed until failure with a forming speed of 0.1 mm/s in the second experiment. Digital twins of the two experiments were created with Simufact Forming 16.0 using the material data characterized and modeled earlier. The middle area of the specimen (Fig. 2), which corresponds to the measuring length, was modeled as a 3D model with elastic–plastic behavior. The 3D space was chosen because it promises a higher degree of accuracy regarding the change in sheet thickness. Further, the 3D model is closer to the intended application of press hardening. The left nodes of the specimen were fixed in all directions and the right nodes were movable only in x-direction (Fig. 12), in which a displacement u_x was applied with the same temporal course as in the experiments. Hexahedral solid-shell elements with five integration points over the thickness arranged as sheet mesh were used to discretize the specimen geometry. A remesher was used, which was initiated when a value of 0.3 was exceeded by the plastic strain. To investigate the influence of the element edge length on the results, a mesh sensitivity study was performed. For this purpose, the element edge length was varied from 1.2 to 0.0375 mm. Beside the characterized material data, 210 GPa is selected for the elastic modulus, 0.3 for the Poisson's ratio and 7.8 kg/dm^3 for the density. The model was calculated implicit with Pardiso–Direct–Sparse solver using four cores. For a validation of the flow curves, the force–displacement–development and the specimen geometry after forming of the first experiment as well as the simulation were compared. To validate the TTT diagram, the retained austenite content of the first experiment was measured with the x-ray diffractometer and correlated to the simulated value. To validate the FLC, the displacement at failure of the second experiment was contrasted with the numerical results.

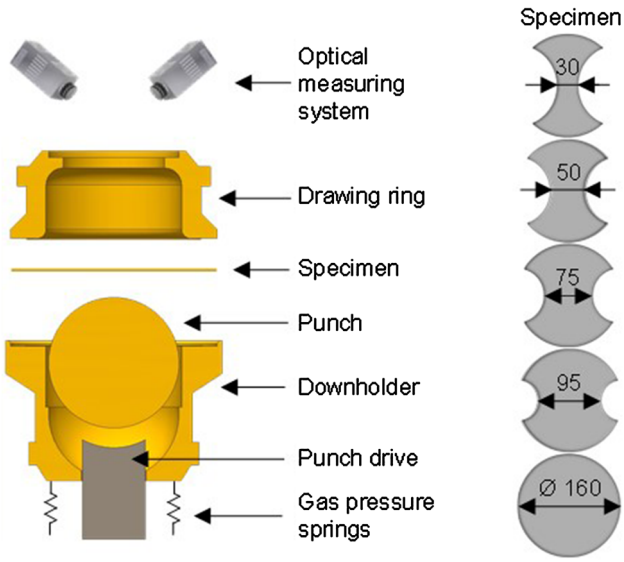

Fig. 4. Schematic representation of the thermal container and of the specimen for performing hot FLC tests (Ref 27)

3. Results

3.1 Material Characterization and Modeling

In Fig. 5, experimental flow curves are shown for a strain rate of 0.1 s^{-1} with a gray underlay (up to a plastic strain of approx. 0.18). In addition, extrapolated flow curves using the combined approach for plastic strains up to 0.6 are depicted. The corresponding indicated parameter of the flow curve extrapolation approaches is listed in Table 1. The decrease in flow stress is clearly visible as the temperature rises. As expected, the hardening behavior of the material is much lower at high temperatures than at lower temperatures.

The experimentally derived CCT diagram of AISI 420C for an austinitization temperature of 1150 °C and a soaking time of 5 min is presented in Fig. 6. Depending on the cooling rate, the formation of pearlitic phase fractions (P), martensite (M) and retained austenite (RA) from the initial austenitic phase is observed. The austenite start temperature Ac_1 was found to be 817 °C, and the austenite finish temperature Ac_3 was 938 °C. By lowering the cooling rate from 50 K/s, a decrease in retained austenite and an increase in martensite as well as pearlitic phase fractions are noticeable. AISI 420C has a particularly low critical cooling rate, around 1 K/s, and the formation of full pearlite phases could not be detected, not even at a cooling rate of 0.1 K/s. The formation of bainite is prevented by the high percentage of the carbide former

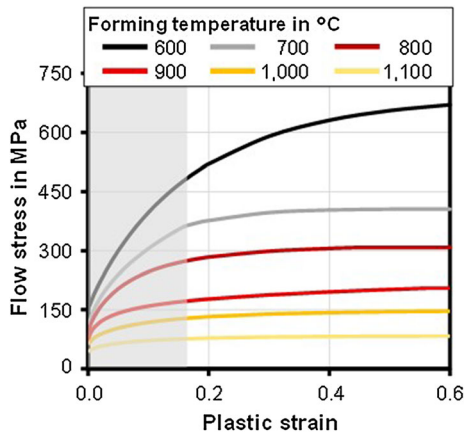

Fig. 5. Experimentally determined (gray overlay) and extrapolated flow curves of AISI 420C with a strain rate of 0.1 s^{-1} for forming temperatures between 600 and 1100 °C

Table 1. Parameters of the flow curve extrapolation approach of AISI 420C for a strain rate of 0.1 s^{-1}

Forming temperature in °C	Parameter							
	β	a_1 in MPa	a_2	a_3	a_4 in MPa	a_5	a_6	$k_{f,0}$ in MPa
600	1E−08	851.68	0.0041	0.33	699.31	− 5.00	0.92	157.93
700	1E−08	513.62	0.0001	0.23	409.93	− 9.79	0.95	110.86
800	1E−08	373.37	0.0001	0.19	310.98	− 7.33	0.78	92.16
900	0.6033	228.42	0.0001	0.16	201.37	− 5.00	0.62	68.56
1000	1E−08	166.89	0.0015	0.15	149.35	− 5.00	0.68	62.34
1100	0.0010	92.29	0.0013	0.11	83.94	− 5.75	0.68	43.97

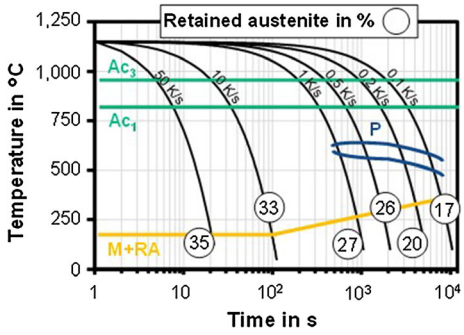

Fig. 6. Experimental CCT diagram of AISI 420C after austenitizing at 1150 °C for 5 min at cooling rates between 50 and 0.1 K/s

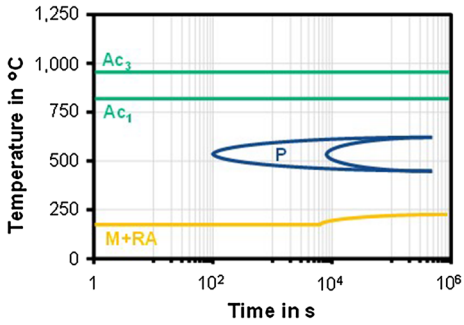

Fig. 7. Experimental-numerically generated TTT diagram of AISI 420C after austenitizing at 1150 °C for 5 min

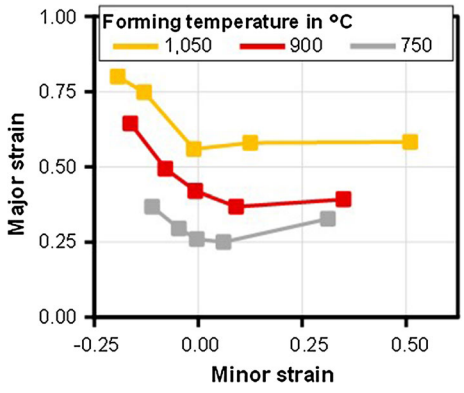

Fig. 8. Experimental-numerically determined hot FLC of AISI 420C for forming temperatures of 750, 900 as well as 1050 °C and 1.5 mm sheet thickness from (Ref 27)

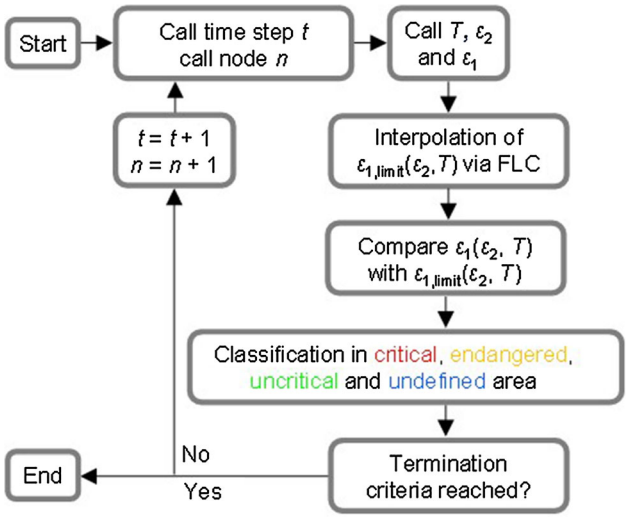

Fig. 9. Flowchart of the subroutine for temperature-dependent failure prediction based on FLC

chromium. This transformation behavior indicates that the material is an air hardener. Furthermore, a martensite finish temperature could not be determined since the martensitic transformation had not been completed even at room temperature. Thus, the samples would have had to be cooled to below room temperature to investigate the martensite finish temperature.

The CCT diagram was converted to a TTT diagram and the generated TTT diagram was manually adjusted until the length change-temperature-functions from experiment and simulation showed a good agreement. Figure 7 shows the finally determined TTT diagram. The Ac_1 and Ac_3 temperatures are given as before. Pearlitic phase fractions (P), martensite (M) and retained austenite (RA) are shown.

The determined major and minor strains at failure using the experimental–numerical method are illustrated in Fig. 8 for five specimen geometries in the range of uniaxial up to biaxial tension. Based on the material data, hot FLC of AISI 420C for forming temperatures of 750, 900 and 1050 °C are interpolated linearly. The FLC tests were performed with specimen of sheet thickness 1.5 mm and the major and minor strains were numerically determined using an element edge length of 0.2 mm. Therefore, the hot FLC are valid for these parameters. Obviously, the highest forming limit is reached at 1050 °C and is reduced with lower forming temperature. In order to be able to use the hot FLC for non-isothermal processes between 750 and 1050 °C in an FE simulation, a post-processing subroutine

is developed to integrate the data in the simulation model. The workflow of the subroutine is illustrated in Fig. 9.

The present temperature T, the present minor strain ε_2 and the present major strain ε_1 are called for each node n at each time step t. The present temperature T is used to interpolate between the different FLC to determine the respective major strain at failure $\varepsilon_{1,\text{limit}}$ for the present minor strain ε_2. In the following, the present major strain $\varepsilon_1(\varepsilon_2,T)$ is compared with the interpolated major strain at failure $\varepsilon_{1,\text{limit}}(\varepsilon_2,T)$ and classified between "undefined", "uncritical", "endangered" and "critical". The classification "endangered" was defined as 90% of the major strain at failure and the undefined rating includes temperatures as well as strains outside the range of the performed material characterization. The subroutine stops as soon as the termination criteria of the simulation, such as the end of forming, are reached.

3.2 Hot Forming FE-Simulation and Validation

Figure 10 and 11 shows the mesh sensitivity for the simulation of the first experiment varying the element edge length from 1.2 to 0.0375 mm. The maximum forming force as well as the effective stress are depicted as a function of the element edge length in Fig. 10 and the plastic strain as well as the retained austenite in Fig 11. The maximum force is the highest for an element edge length of 1.2 mm and decreases with the element edge length. The effective stress and the plastic strain, on the other hand, are underestimated for an element edge length of 1.2 mm and increase as the element edge length decreases. In comparison, the retained austenite content amounts to 33.2% for all element edge lengths. With an element edge length of 0.15 mm, the difference to the element edge length of 0.075 mm is less than 1% for the maximum force and the effective stress. As is well known, the plastic strain increases continuously with a reduction in the element edge length, which is clearly visible here. Since the FLC were determined for an element edge length of 0.2 mm, the comparison to the experimental values is performed for the element edge length of 0.15 mm for the best agreement.

A comparison of the numerical and experimental results of the first experiment is given in Fig. 12 and 13. In the simulation of the tensile test, only the middle section of the specimen is considered according to the experimental boundary conditions. In Fig. 12, the thickness distributions of the simulated specimen and a tested specimen are depicted. The width and thickness before testing were 3 and 1.5 mm. At the thinnest part

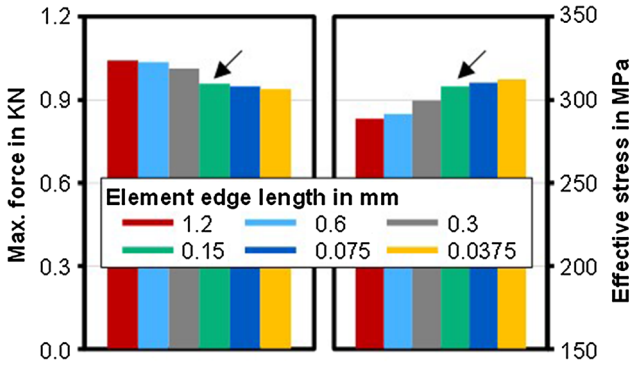

Fig. 10. Mesh sensitivity analysis for a variation of the element edge length from 1.2 to 0.0375 mm and its influence on the maximum force as well as the effective stress.

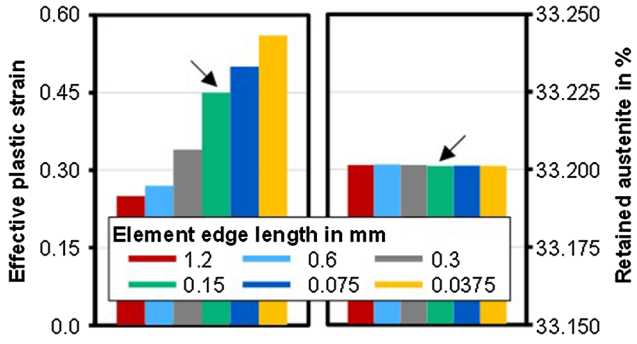

Fig. 11. Mesh sensitivity analysis for a variation of the element edge length from 1.2 to 0.0375 mm and its influence on the plastic strain as well as the retained austenite

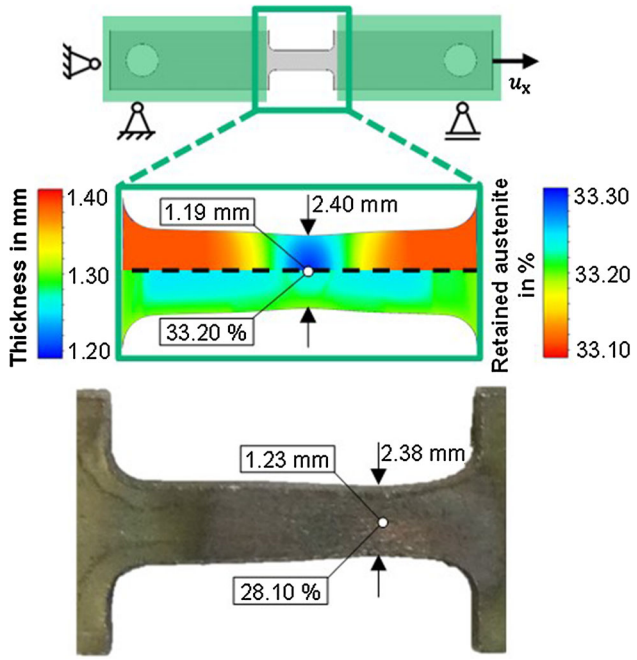

Fig. 12. Comparison of the numerical and experimental specimen geometries as well as the retained austenite content for the first experiment

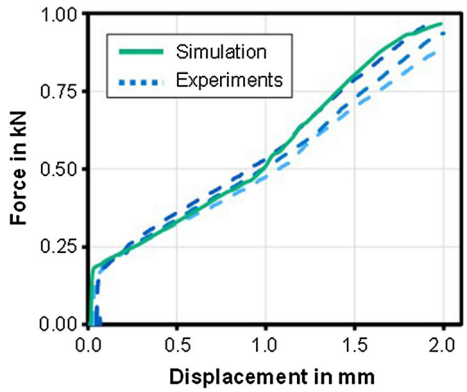

Fig. 13. Comparison of the numerical and experimental force–displacement–development for the first experiment

of the specimen, the width is 2.40 mm and the thickness 1.19 mm. The experimental values were measured optically by means of a microscope and are 2.38 mm as well as 1.23 mm. The difference in width is therefore less than 0.1% and in thickness 0.3%.

A comparison of the numerical and the three experimental force–displacement–developments is shown in Fig. 13. Again, a high conformity between simulation and experiment is given. It can therefore be concluded that the flow-behavior characterization and the extrapolation worked successfully. The slightly faster increase in force for the simulation after 1 mm displacement is due to the fact that the flow curves were extrapolated marginally too steep.

The retained austenite contents of the simulated specimen and of the experimental test are also depicted in Fig. 12. It amounts to 33.2% for the simulation and to 28.1% for the experiment in the middle of the testing area. This deviation of about 15% can be explained by the fact that the influence of forming on the microstructural transformation has not been taken into account in the simulation model. A deformation in the austenitic material can shift the phase areas of the TTT diagram to lower times and higher temperatures so that phase transformations and martensite formation already take place at higher cooling rates (Ref 2). Accordingly, more martensite and less retained austenite than in the simulation are developed in the experiment due to the forming operation. The calculation time for the simulation of the first experiment was 59 minutes for an element edge length of 0.15 mm.

A comparison of the numerical and experimental results of the second experiment is given in Fig. 14. The simulated specimen geometry with indication of the critical forming limit is displayed for the occurrence of failure over the entire sheet thickness at a displacement of 2.54 mm. An experimental specimen is depicted below the simulations. The experimental displacement amounts to 2.79 mm.

The agreement of simulation and experiment concerning the displacement at the point of material failure is satisfactory. The deviation of about 8% can be explained by the fact that the hot FLC could not be recorded without friction. Understandably, it has been observed that lubrication between the punch and the specimen is problematic at high temperatures (Ref 27). The material fails earlier with higher friction. While testing a tensile specimen there is no contact between the testing area and the tools. Thus, no friction is present so that the forming capacity is not reduced. Therefore, material failure is indicated slightly prematurely in the simulation of the tensile test compared to the experiment, since the FLC are recorded with friction. The calculation time for the simulation of the second experiment using the subroutine was 49 minutes for an element edge length of 0.15 mm.

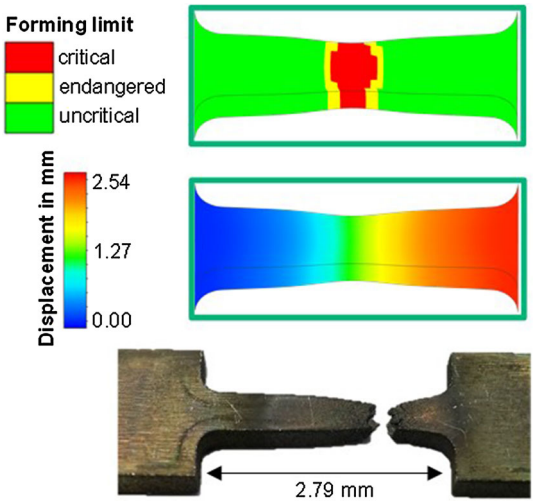

Fig. 14. Comparison of numerical and experimental specimen geometries at fracture for the second experiment

4. Conclusions

This article presents new methods for material characterization and numerical modeling of processes involving the new press hardening steel AISI 420C. The material behavior regarding flow properties, phase transformation as well as forming limit was characterized for process-relevant parameters and modeled using experimental–numerical approaches. For an evaluation and a first validation of the material model created, numerical simulations of the hot-formed tensile specimens were carried out and compared to experimental results with good agreement. In future work, the material model will be used to simulate press hardening of a B-pillar demonstrator geometry, which is close to a crash-relevant car body part. For this purpose, experimental press hardening tests will be performed. Further validations of the material model will be executed by comparing and analyzing the demonstrator parts regarding final part geometry, resulting phase fractions as well as failure prediction.

Acknowledgments

The authors gratefully acknowledge the support of the German Research Foundation (Deutsche Forschungsgemeinschaft, DFG) within the Project 385989694 "Determining the forming limits of martensitic chromium steels for hot forming." Further we thank Outokumpu Nirosta GmbH for providing the martensitic chromium steel AISI 420C for the investigations.

Funding

Open Access funding enabled and organized by Projekt DEAL.

References

1. H. Karbasian and A.E. Tekkaya, A Review on Hot Stamping, *J. Mater. Process. Technol.*, 2010, **210**(15), p 2103–2118

2. B.-A. Behrens, K. Brunotte, H. Wester, and E. Stockburger, Investigation of the Process Window for Deformation Induced Ferrite to Improve the Joinability of Press-Hardened Components, in *Proceedings 29th International Conference on Metallurgy and Materials*, Brno, Czech Republic, 2020, p 579–584
3. M. Dahmen, V. Janzen, S. Lindner and R. Wagener, Laser Beam Welding of Ultra-high Strength Chromium Steel with Martensitic Microstructure, *Phys. Procedia*, 2014, **56**(1), p 525–534
4. B.-A. Behrens, S. Jüttner, K. Brunotte, F. Özkaya, M. Wohner and E. Stockburger, Extension of the Conventional Press Hardening Process by Local Material Influence to Improve Joining Ability, *Procedia Manuf.*, 2020, **47**(1), p 1345–1352
5. H. Karbasian and A.E. Tekkaya, A Review on Hot Stamping, *J. Mater. Process. Technol.*, 2010, **210**, p 2103–2118
6. M. Merklein, M. Wieland, M. Lechner, S. Bruschi and A. Ghiotto, Hot Stamping of Boron Steel Sheets with Tailored Properties: A Review, *J. Mater. Process. Technol.*, 2016, **228**, p 11–24
7. K. Mori, P.F. Bariani, B.-A. Behrens, A. Brosius, S. Bruschi, T. Maeno, M. Merklein and J. Yanagimoto, Hot Stamping of Ultra-High Strength Steel Parts, *CIRP Ann. Manuf. Technol.*, 2017, **66**, p 755–777
8. P. Åkerström, G. Bergman and M. Oldenburg, Numerical Implementation of a Constitutive Model for Simulation of Hot Stamping, *Modell. Simul. Mater. Sci. Eng.*, 2007, **15**, p 105–119
9. B.-A. Behrens, K. Brunotte, H. Wester, and F. Müller, Practical Process Characterisation for Hot-Stamping Regarding the Heat Transfer Coefficient using a Numerical and Experimental Coupled Method, in *Proceedings 29th International Conference on Metallurgy and Materials*, Brno, Czech Republic, 2020, p 573–578
10. J. Venemaa, E. Atzemaa, J. Hazratib, D. Matthewsc and T. van den Boogaard, Modelling of Friction in Hot Stamping, *Procedia Manuf.*, 2020, **47**, p 596–601
11. L. Deng, S. Mozgovoy, J. Hardell, B. Prakash and M. Oldenburg, Numerical Study of Contact Conditions in Press Hardening for Tool Wear Simulation, *Int. J. Mater. Form.*, 2017, **10**, p 717–727
12. A. Paul, F. Reuther, S. Neumann, A. Albert and D. Landgrebe, Process Simulation and Experimental Validation of Hot Metal Gas Forming with New Press Hardening Steels, *J. Phys. Conf. Ser.*, 2017, **896**, p 1–8
13. Y. Chen, S. Li, Y. Li, Y. Wang, Z. Li and Z. Li, Constitutive Modeling of TA15 Alloy Sheet Coupling Phase Transformation in Non-isothermal Hot Stamping Process, *J. Market. Res.*, 2021, **12**, p 629–642
14. A. Birkert, S. Haage and M. Straub, *Umformtechnische Herstellung Komplexer Karosserieteile—Auslegung von Ziehanlagen*, 1st ed. Springer, Berlin, 2013
15. W.A. Johnson and R.F. Mehl, Reaction Kinetics in Processes of Nucleation and Growth, *Trans. Am. Inst. Min. Metall. Eng.*, 1939, **135**(1), p 416–442
16. D.P. Koistinen and R.E. Marburger, A General Equation Prescribing the Extent of the Austenite-Martensite Transformation in Pure Iron-Carbon Alloys and Plain Carbon Steels, *Acta Metall.*, 1959, **7**(1), p 59–60
17. B.-A. Behrens, J. Schröder, D. Brands, L. Scheunemann, R. Niekamp, A. Chugreev, M. Sarhil, S. Uebing and C. Kock, Experimental and Numerical Investigations of the Development of Residual Stresses in Thermo-Mechanically Processed Cr-Alloyed Steel 1.3505, *Metals*, 2019, **9**(4), p 1–28
18. D. Banabic, *Sheet Metal Forming Processes—Constitutive Modelling and Numerical Simulation*, 1st ed. Springer, Berlin, 2010
19. D. Pellegrini, J. Lechler, A. Ghiotti, S. Bruschi and M. Merklein, Comparison of Forming Limit Curves for Hot Stamping of High Strength Steels, *Key Eng. Mater.*, 2009, **410–411**(1), p 297–304
20. Standard ISO 6892-1:2020-06, *Metallic Materials—Tensile Testing—Part 1: Method of Test at Room Temperature*, Beuth Verlag GmbH, Berlin, 2020
21. H.W. Swift, Plastic instability under plane stress, *J. Mech. Phys. Solids*, 1952, **1**(1), p 1–18
22. J.E. Hockett and O.D. Sherby, Large strain deformation of polycrystalline metals at low homologous temperatures, *J. Mech. Phys. Solids*, 1975, **23**(2), p 87–98
23. ASTM A1033-18, *Standard Practice for Quantitative Measurement and Reporting of Hypoeutectoid Carbon and Low-Alloy Steel Phase Transformations*, ASTM International, West Conshohocken, 2018
24. B.-A. Behrens, A. Chugreev and C. Kock, Experimental-Numerical Approach to Efficient TTT-Generation for Simulation of Phase Transformations in Thermomechanical Forming Processes, *IOP Conf. Ser. Mater. Sci. Eng.*, 2018, **461**(1), p 1–6
25. Standard ISO 12004-2:2019-06, *Metallic Materials, Sheet and Strip, Determination of Forming Limit Curves—Part 2, Determination of Forming Limit Curves in the Laboratory*, Beuth Verlag GmbH, Berlin, 2019
26. V. Hasek, Anwendung von Grenzformänderungsschaubildern, *Industrie-Anzeiger*, 1997, **99**(20), p 343–347
27. B.-A. Behrens, J. Uhe, H. Wester, and E. Stockburger, Hot Forming Limit Curves for Numerical Press Hardening Simulation of AISI 420C, in *Proceedings 29th International Conference on Metallurgy and Materials*, Brno, Czech Republic, 2020, p 350–355